

DARK MATTER AND BARYONS IN THE MOST X-RAY LUMINOUS AND MERGING GALAXY CLUSTER RX J1347.5–1145^{*}

MARUŠA BRADAČ^{1,2,x}, TIM SCHRABBACK³, THOMAS ERBEN³, MICHAEL MCCOURT¹, EVAN MILLION¹, ADAM MANTZ¹, STEVE ALLEN¹, ROGER BLANDFORD¹, ALEKSI HALKOLA³, HENDRIK HILDEBRANDT³, MARCO LOMBARDI^{4,5}, PHIL MARSHALL², PETER SCHNEIDER³, TOMMASO TREU^{2,y}, JEAN-PAUL KNEIB⁶

Draft version March 27, 2008

ABSTRACT

The galaxy cluster RX J1347.5–1145 is one of the most X-ray luminous and most massive clusters known. Its extreme mass makes it a prime target for studying issues addressing cluster formation and cosmology. Despite the naive expectation that mass estimation for this cluster should be straightforward (high mass and favorable redshift make it an efficient lens, and in addition it is bright in X-rays and appears to be in a fairly relaxed state), some studies have reported very discrepant mass estimates from X-ray, dynamical and gravitational lensing. In this paper we present new high-resolution HST/ACS and Chandra X-ray data. The high resolution and sensitivity of ACS enabled us to detect and quantify several new multiply imaged sources, we now use a total of eight for the strong lensing analysis. Combining this information with shape measurements of weak lensing sources in the central regions of the cluster, we derive a high-resolution, absolutely-calibrated mass map. This map provides the best available quantification of the total mass of the central part of the cluster to date. We compare the reconstructed mass with that inferred from the new Chandra X-ray data, and conclude that both mass estimates agree extremely well in the observed region, namely within $400h_{70}^{-1}$ kpc of the cluster center. In addition we study the major baryonic components (gas and stars) and hence derive the dark matter distribution in the center of the cluster. We find that the dark matter and baryons are both centered on the BCG within the uncertainties (alignment is better than < 10 kpc). We measure the corresponding 1-D profiles and find that dark matter distribution is consistent with both NFW and cored profiles, indicating that a more extended radial analysis is needed to pinpoint the concentration parameter, and hence the inner slope of the dark matter profile.

Subject headings: cosmology: dark matter – gravitational lensing – galaxies:clusters:individual:RX J1347.5-1145

1. INTRODUCTION

Galaxy clusters have been the focus of very intense research over the past decade. They are extremely valuable for studying the empirical properties of dark matter, as well as for exploring the growth of structure at the high mass tail of the mass function. The mass distribution of galaxy clusters is particularly important for cosmological studies because it provides a critical test of the Cold Dark Matter (CDM) paradigm and constrain dark energy models, if their mass and its distribution is reliably

Electronic address: marusa@physics.ucsb.edu

^{*} Based on observations made with the NASA/ESA Hubble Space Telescope, obtained at the Space Telescope Science Institute, which is operated by the Association of Universities for Research in Astronomy, Inc., under NASA contract NAS 5-26555. These observations are associated with program # 10492. This work is also based on observations collected at the European Southern Observatory, Chile (ESO program 078.A-0746(A)).

¹ Kavli Institute for Particle Astrophysics and Cosmology, 2575 Sand Hill Rd. MS29, Menlo Park, CA 94025, USA

² Department of Physics, University of California, Santa Barbara, CA 93106, USA

³ Argelander-Institut für Astronomie, Auf dem Hügel 71, D-53121 Bonn, Germany

⁴ European Southern Observatory, Karl-Schwarzschild-Str. 2, D-85748 Garching, Germany

⁵ Università degli Studi di Milano, v. Celoria 16, I-20133 Milano, Italy

⁶ OAMP, Laboratoire d'Astrophysique de Marseille UMR, 6110 Traverse du Siphon, 13012 Marseille, France

^x Hubble Fellow

^y Sloan Fellow, Packard Fellow

determined. However, in some cases the cluster mass estimates from the weak lensing, strong lensing and X-ray measurements disagree: the origin of these discrepancies is likely to be a combination of erroneous assumption of the cluster potential, projection effects and complicated gas physics not taken into account. In addition, systematic effects like cluster member contamination and unknown redshift distribution of sources, strong lensing image identification, temperature calibration, etc. enter the error budget for X-ray and lensing analyses.

It was first proposed by Navarro et al. (1997) that the dark matter halos on a variety of scales should follow a universal profile within the currently accepted Λ CDM paradigm. The 3-D density distribution of dark matter should follow $\rho_{\text{DM}} \propto r^{-1}$ within a scale radius r_s and falls off steeper at radii beyond that ($\rho_{\text{DM}} \propto r^{-3}$). However recent simulations have shown that the profile might be modified and the structural parameters vary with redshift and mass (Neto et al. 2007; Navarro et al. 2004). In addition, likely interaction between dark matter and baryons further complicate the picture (Gnedin et al. 2004; Nagai & Kravtsov 2005). It is therefore crucial to compare simulations and observations keeping the baryonic component in mind. This will allow us to measure the slopes of dark matter profiles, which is a critical test for our currently accepting cosmology as well as understanding the complicated baryonic physics in galaxy clusters. Several works have previously studied mass distribution in number of clusters using com-

blended strong and weak lensing reconstruction (see e.g. Natarajan & Kneib 1996; Kneib et al. 2003; Smith et al. 2004; Diego et al. 2005; Cacciato et al. 2005; Jee et al. 2007; Limousin et al. 2007) and combined strong lensing and stellar kinematics data of the dominating central galaxy (Sand et al. 2007). These approaches offer valuable extra constraints for determining the mass distributions.

In this paper we study the most luminous X-ray clusters known to date. The cluster RX J1347.5–1145 (Schindler et al. 1995) at a redshift $z = 0.451$ has been a subject of intense past research. Rich datasets including X-ray (Schindler et al. 1995, 1997; Allen et al. 2002; Ettori et al. 2004; Gitti & Schindler 2004; Gitti et al. 2007) and optical (Fischer & Tyson 1997; Sahu et al. 1998; Cohen & Kneib 2002; Ravindranath & Ho 2002) as well as observations of Sunyaev-Zel'dovich (SZ) effect (Pointecouteau et al. 2001; Komatsu et al. 2001; Kitayama et al. 2004) have been obtained, yet the mass determinations based on X-ray properties, SZ effect (SZE), velocity dispersion measurement, strong and weak lensing have many times yielded discrepant results (see Cohen & Kneib 2002 for a summary). In particular the discrepancy between the dynamical mass estimate (Cohen & Kneib 2002), early X-ray mass measurements (Schindler et al. 1997) and lensing results (Fischer & Tyson 1997) yielded a factor of ~ 3 discrepancy in their mass estimates.

Cohen & Kneib (2002) suggested the cluster is likely undergoing a major merger which would reconcile the low velocity dispersion (and hence virial mass) measurement and its high mass as predicted by gravitational lensing and X-ray data. If the velocity dispersion measures predominately one component, and the X-ray gas has virialized to the post-merger cluster mass, this can possibly explain the data. Further evidence for a merger scenario comes also from the optical morphology: the cluster contains two cD galaxies (see e.g. Fig. 1 - throughout this paper we will refer to the brighter, western one as the BCG, and the other as the second cD). Finally, there is a region of shocked gas in the south-east quadrant discovered and discussed by Komatsu et al. (2001) (with SZ effect) and Allen et al. (2002) based on X-ray observations with Chandra. We confirm the latter using the newest Chandra X-ray data.

In order to resolve the puzzle of mass estimates in Bradač et al. (2005a) we studied this cluster using ground-based optical data, and for the first time determined its mass distribution using a combined strong (multiply-imaged systems) and weak (statistical measurement using shape information of an ensemble of background galaxies) gravitational lensing analysis. The main drawback of that reconstruction was the lack of clearly identified multiply imaged systems and their redshifts. In the current paper we obtained new multi-color HST/ACS data. The high resolution and sensitivity of ACS allowed us to unambiguously identify many new multiply imaged systems. In this analysis we are able to use 9 multiply imaged systems, in contrast to the single one of Bradač et al. (2005a). Furthermore the far greater density of sources that can be used for weak lensing (a factor of 5 improvement) has allowed us to obtain an absolutely-calibrated mass map at high resolution. We also present new X-ray data and compare estimates from

both analyses. In addition we describe a new automated search routine for multiply imaged sources we are currently developing; its main advantage is that it combines colors and information on lensing geometry of the whole system to obtain matching pairs in a semi-automated way.

Our final mass reconstruction is again performed using a pixelated model which combines the information from strong and weak gravitational lensing. If spectroscopic redshifts of the multiply imaged systems were available, this would fully eliminate the need of using models that assume a particular shape of the gravitational potential. However, since only one system has a spectroscopically confirmed redshift, we use the predictive power of gravitational lensing to predict the redshifts for the remaining systems. As explained further in §3, we therefore model strong lensing data using parametrised models at the start to obtain the redshifts. For the final reconstruction we however do not assume a special shape of the gravitational potential, instead exploring a much larger range of cluster mass distributions and profiles (provided the estimated redshifts are reasonably reconstructed). Furthermore, we use cluster to study the interplay between baryons and dark matter, therefore we study separately its stellar, gas and dark matter component. This allows us to measure the cluster's dark matter profile, one of the strong predictions of Λ CDM cosmology.

This paper is structured as follows. In section 2 we describe the optical data used in this analysis. The basic image processing and the extraction of the strong gravitational lensing data is described in section 3 and in section 4 we describe the weak gravitational lensing data. We present the X-ray data in section 5. We infer the mass distribution of the cluster RX J1347.5–1145 from lensing data, and compare it with X-ray data, in section 6. The individual contributions of stars, gas, and dark matter to the total mass of the cluster are studied in section 7. The conclusions are presented in section 8. To evaluate the angular diameter distances throughout the paper we assume the Λ CDM cosmology with $\Omega_m = 0.3$, $\Omega_\Lambda = 0.7$, and Hubble constant $H_0 = 70 \text{ km s}^{-1} \text{ Mpc}^{-1}$.

2. OPTICAL OBSERVATIONS AND INITIAL DATA REDUCTION PROCESS

ACS/WFC imaging of the cluster RX J1347.5–1145 was carried out in Cycle 14 (proposal 10492, PI Erben) on 2006 March 9–11. The cluster was observed in a single (dithered) pointing and three different filters F475W, F814W, and F850LP for 5280s (two orbits) each. The demands placed by the lensing analysis require special care when reducing the images. We base the reduction on the bias and flat-field corrected flt-images (provided by the standard ACS pipeline). For each exposure we compute a noise model including all noise sources *except* object photon noise, and update the bad pixel mask as detailed in Marshall et al. (in preparation). We subtract the sky background separately in the four image quadrants to correct for the sometimes present residual bias level. Satellite trails are masked manually, in order to exclude them from the coaddition. We use the *Multidrizzle* (Koekemoer et al. 2002) routine to align the images, correct for geometric camera distortion, mask cosmic rays, and for coaddition. To register the images with the astrometric accuracy needed for the lensing analysis, we

determine the offsets among the images by matching windowed **SExtractor** (Bertin & Arnouts 1996) positions of high S/N objects in the individual, distortion-corrected exposures. We calculate residual shifts and rotations using the IRAF routine **geomap**, which are then fed back into **Multidrizzle**. We use “square” as the final drizzling kernel, where we slightly shrink the input pixels ($\text{pixfrac} = 0.9$) and set the output pixel scale to 0.03 arcsec. This is smaller than the original pixel scale of the ACS/WFC detector in order to reduce the impact of resampling on the shape measurements. In the final coaddition, we use our noise model for inverse variance weighting. For further details on the data reduction see Marshall et al. (in preparation).

3. STRONG LENSING DATA ANALYSIS AND FITTING PARAMETRISED MODELS

With the advent of the high resolution HST optical images the quality and complexity of the strong lensing data increased dramatically. Many clusters have been observed with HST showing numerous multiply imaged systems (the most notable example being A1689 – Broadhurst et al. 2005; Halkola et al. 2006). By far the most time-consuming part of the strong analysis is, however, to match the multiply imaged system - i.e. identify all the multiple images that were produced for a single source.

First steps in trying to optimise this process were done by Kneib et al. (1993) and Sharon et al. (2005). Their methods still involve significant human involvement; we are aiding the process of searching for multiple image systems with automated color and geometry matching. Our method is currently under development and once finished will allow for simultaneous search of the best matching objects in the color space as well as including the geometry of the system (i.e. positions and orientations of the lensed images). This is a very important step in the view of large samples of galaxy clusters that will be discovered and targeted in the future optical surveys (such as SNAP, LSST, DUNE and PanSTARRS).

We start by considering a simple initial guess for a cluster potential together with a hypothesis of at least one multiple image system. We use the image positions to determine the mass distribution of the cluster using a simple parametric model. The image positions (at the end of this process we use all images listed in Table 1 and shown in Fig. 1) are used in **LENSTOOL**, (<http://www.oamp.fr/cosmology/lenstool/>, Kneib et al. 1993). The code determines the best fit parameters of a parametrised model. In addition, its Bayes optimization and Monte Carlo Markov Chain (MCMC) sampling routines (Jullo et al. 2007) allow us to obtain a set of all models that satisfactorily fit the data (for few model parameters, such as the mass and ellipticity of the cluster). We characterize RX J1347.5–1145 by two PIEMD profiles (see e.g. Limousin et al. 2005; Elíasdóttir et al. 2007 for the basic properties of the model), centered on the two brightest cluster members. In addition we also include the 20 brightest cluster members in the I-band to the mass model. They are each modelled as PIEMD spheres with a line-of-sight velocity dispersion σ_{PIEMD}^g and cut radius $r_{\text{cut,PIEMD}}^g$ proportional to the luminosity L of each member ($\sigma_{\text{PIEMD}}^g \propto L^{1/4}$ and $r_{\text{cut,PIEMD}}^g \propto L^{1/2}$). The best-fit

scaling was found to be $\sigma_{\text{PIEMD}}^g = (260 \pm 50) \text{ km s}^{-1}$ and $r_{\text{cut,PIEMD}}^g = (5 \pm 1) \text{ kpc}$ for a galaxy with $m_I = 20.5$. In total this adds to 50 constraints and 34 free parameters (42 when including unknown redshifts).

The parameters of the best-fit model (using the final catalogue of all multiply imaged systems) are listed in Table 2. The ellipticities of the two main components are given as the ratio of minor/major axis (b/a) and the position angle ϕ measured west-through-north. The parametrised model predicts the images with an average accuracy of 3''. The least well predicted image system is the image system F, which is however perturbed by one of the cluster members (included in the model only as one of the 20 cluster members and not minimized for individually). The two main components have very similar velocity dispersions, however as discussed extensively in Halkola et al. (2008) given the degeneracies in the modelling, this is not the only solution for this cluster.

We justify the choice of a two component model by comparing the Bayesian evidence (for details see Kneib et al. 2003; Jullo et al. 2007) when fitting one or two PIEMD components (both times including the cluster members to the fit, and letting all the parameters of one or both PIEMD components to vary). The logarithmic evidence is a factor of 3 larger in the case of a two component model, thereby clearly justifying the two-clump model used for the fit.

Using the samples (i.e. a set of models that satisfactory fits the data) we then predict possible additional images for the initial guess system and matches to further (not necessarily yet identified as multiple) images. This allows us to find a region in space, where matches to known systems and objects should be searched for. Further, if a match in color space is found, the hypothesis that it is a multiply imaged system can be tested and the redshift estimate is obtained using the improved lens model.

All the identified images were visually inspected (we are hoping to be able to omit this step altogether in the future).

3.1. Redshifts for Strongly Lensed Systems

For RX J1347.5–1145 the only multiply imaged system with confirmed spectroscopic redshift is system A (Table 1 and Fig. 1). The redshift of the brighter of the two images was independently measured to be 1.75 for both images with FORS spectroscopic data (Lombardi et al. 2007) as well as Keck data. This is in agreement with the photometric redshift obtained from UBVRIJHKs ground-based data in Bradač et al. (2005a), where a redshift 1.76 ± 0.1 was used for this system. We have predicted the redshifts of the other identified systems by setting them as free parameters when the system was added in the image identification procedure outlined above. The resulting best-fit redshifts are given in Table 1. The final error bars were obtained by source-plane modelling (modelling in the image-plane with all the parameters set free would be too time consuming) and should be treated as approximate.

Ideally, the unknown redshift should be fitted simultaneously with weak and strong lensing data using the method described in §6 (which does not assume a specific model family for the cluster potential). This is unfortunately not possible due to the so-called mass-sheet degeneracy (Falco et al. 1985; Schneider & Seitz 1995).

TABLE 1
THE PROPERTIES OF THE
MULTIPLY-IMAGED SYSTEMS USED IN THIS
WORK. THE REDSHIFT OF THE SYSTEM A
WAS OBTAINED USING FORS SPECTRA,
WHEREAS THE OTHERS HAVE BEEN
DETERMINED BY LEAVING THEM AS FREE
PARAMETERS WHEN FITTING STRONG
LENSED DATA WITH PARAMETRISED
MODEL.

	Ra	Dec	z_{pred}
A	206.87207	-11.761072	1.75
	206.88263	-11.764407	
B	206.87250	-11.746470	1.2 ± 0.1
	206.87117	-11.748356	
	206.87316	-11.745810	
C	206.87423	-11.745110	2.0 ± 1.0
	206.88293	-11.741210	
	206.88415	-11.741798	
D	206.87845	-11.749200	2.2 ± 0.1
	206.87833	-11.749682	
	206.87219	-11.765260	
E	206.87406	-11.766258	2.5 ± 0.6
	206.86549	-11.764203	
	206.86661	-11.765704	
F	206.86395	-11.755330	4.0 ± 2.0
	206.87357	-11.768255	
	206.87130	-11.767085	
G	206.88088	-11.770223	3.0 ± 0.5
	206.86634	-11.766999	
	206.86714	-11.742389	
H	206.88754	-11.757578	4.2 ± 1.0
	206.88513	-11.748397	
	206.87878	-11.753372	
I	206.87765	-11.759400	1.7 ± 0.2
	206.86960	-11.747372	

This transformation essentially allows us to determine the surface mass density only up to a constant (that enters in a re-scaling and offset of the surface mass density). Since the redshift information enters the lensing equation in similar fashion (see Bradač et al. 2004 for more details), if only a *single* redshift of multiply imaged system is known, without assuming a parametrized model, the rest of the redshifts can not be determined. Weak lensing in principle should provide a second redshift plane and hence constrain the profile and its normalisation, allowing us to reconstruct the data without the need of any simple parametrised modelling. In practice, however, the weak lensing data is noisy and therefore not sufficient to break the mass sheet degeneracy (see e.g. Bradač et al. 2004; Limousin et al. 2007). If one tries to constrain the unknown redshift of a system with images far away from the images with known redshift, one can obtain equally good fits by either slightly perturbing the potential or by changing the redshift. Hence we need to use parametrized models for this part of the analysis. However, when other multiply imaged systems are present in the vicinity, the redshift can still be determined using the pixelated model; when we added image system I we could only get a good fit with $z = 1.7$ and not the photometric redshift estimate of $z = 2.2$; the same conclusion was obtained already by Halkola et al. 2008.

4. WEAK LENSING DATA ANALYSIS

We perform the weak lensing shape measurements on the F814W data due to their higher galaxy num-

TABLE 2
RESULTS OF BEST-FIT PARAMETRIC MODELLING OF STRONG LENSING
DATA (PARAMETERS REFER TO THE VALUES USED BY LENSTOOL,
AXIS-RATIO b/a AS THAT OF THE PROJECTED MASS DISTRIBUTION).

	σ_{PIEMD} (km s^{-1})	r_c (kpc)	r_{cut} (kpc)	b/a	ϕ
BCG	1640 ± 40	340 ± 30	1000 ± 30	0.89 ± 0.01	$16^\circ \pm 1^\circ$
2nd cD	1640 ± 10	400 ± 5	2000 ± 60	0.87 ± 0.01	$70^\circ \pm 1^\circ$

ber density. For the PSF anisotropy and smearing correction we closely follow the technique described in Schrabback et al. (2007). The procedure is based on the KSB+ algorithm (Kaiser et al. 1995; Luppino & Kaiser 1997; Hoekstra et al. 1998), which has extensively been tested on the simulations of the STEP collaboration (Heymans et al. 2005; Massey et al. 2007). The KSB+ method is formally valid only in the weak lensing regime, however as discussed in Bradač et al. (2006) (see also Massey & Goldberg 2007) the approach is also valid in the non-weak lensing regime to the accuracy needed here. We select stars from the half-light-radius vs. magnitude diagram.

In contrast to Bradač et al. (2006) we use the new PSF correction scheme developed by Schrabback et al. (2007). The method is superior, since it takes the temporal (as well as the spatial) variability of the ACS PSF into account. The PSF variation is measured from stars in individual exposures (rather than in the co-added image as was traditionally done). It is then compared with star-rich fields from archival observations (stellar templates). The shapes of the stars in individual exposures of our data set are first compared to the shapes of stars from stellar templates and the best template is chosen. The full PSF model is then composed of several templates; such a model therefore captures the full spatial as well as temporal variability of ACS. We detect short-term variations of the ACS PSF, which are interpreted as focus changes due to thermal breathing of the telescope (see also Schrabback et al. 2007; Krist 2003; Rhodes et al. 2007; Anderson & King 2006). The detailed PSF model obtained from this procedure is then used to correct the shapes of all the objects in the RX J1347.5–1145 field.

Finally, since the PSF shape of stars changes as a function of the scale at which we use for the shape measurement (see e.g. Heymans et al. 2005; Jee et al. 2006), we match the scale used for PSF and galaxy shape measurement. This method reduces the systematic contribution to the shear correlation functions due to PSF distortions to $< 2 \times 10^{-6}$ for galaxy fields containing at least 10 stars, and was demonstrated to be sufficient even for cosmic shear measurements (Schrabback et al. 2007), where the signal is more than an order of magnitude smaller than measured in cluster fields. In addition, we apply a parametric model, similarly to the one proposed by Rhodes et al. (2007), to correct for the influence of the degraded charge-transfer-efficiency on galaxy shapes, see Schrabback et al. (in prep.) for further details. Using simulated weak lensing data from the STEP1 project (Heymans et al. 2006), we identified a constant bias between the input and measured shear values. In the analysis of the STEP2 data we correct for this bias by the introduction of a multiplicative shear calibration

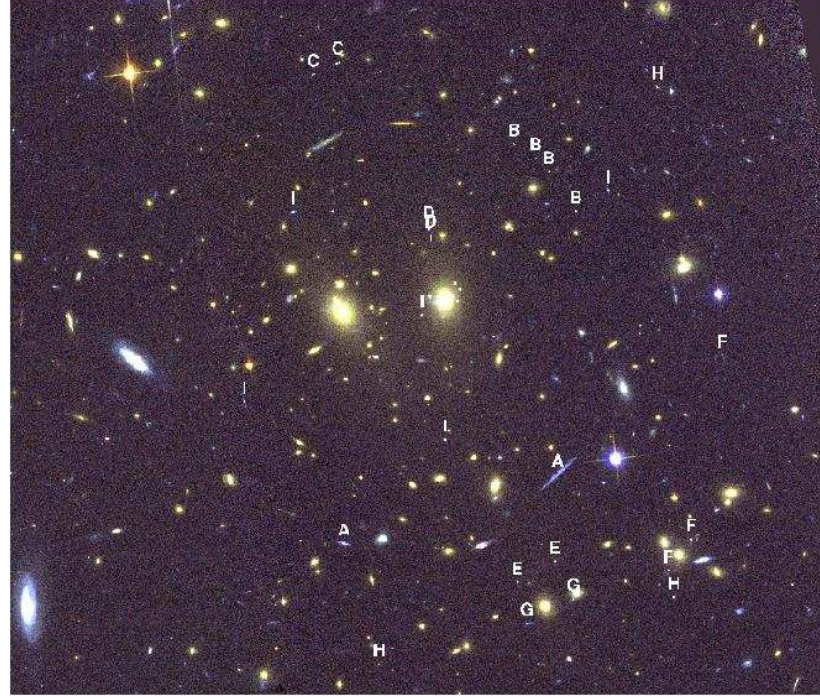


FIG. 1.— The F450W-F814W-F850LP color composite of the cluster RX J1347.5–1145. Multiply imaged systems are marked and labeled (see also Table 1). North is up and East is left, the field is $2.3' \times 2.3'$, which corresponds to $800 \times 800 \text{ kpc}^2$ at the redshift of the cluster. The color composite was created following the algorithm from Lupton et al. (2004).

factor of 1.10, which prove to be on average accurate at the $\sim 2\%$ level also for this different set of image simulations (Massey et al. 2007). In the analysis of the RX J1347.5–1145 data we apply slightly different galaxy selection criteria, leading to a marginally changed calibration factor of 1.08, which we apply to the data.

To exclude cluster members from the final catalog we match it to the photometric redshift catalog from the ground-based (VLT/FORS and ISAAC) data from Bradač et al. (2005a). We exclude all the galaxies having measured photometric redshifts $z_{\text{phot}} < 0.5$. Unfortunately, however, we can not use the photometric redshift estimates for all the object in the weak lensing catalog, since many of the faint objects were undetected or unresolved in the ground-based data. Therefore following the prescription of Schrabback et al. (2007) we use the GOODS-MUSIC sample and apply the corresponding magnitude cuts to the data and obtain the average redshift for galaxies in the weak lensing catalogue of $z_{\text{WL}} = 1.4$. The exact value we use has little importance (as discussed in §6.3) on the final mass reconstruction, since the weak lensing signal/noise is much lower than the strong lensing one, and therefore the mass scaling is determined predominately by the strong lensing systems. This is however only true for the regions where we reconstruct the mass, once we extend the measurements far outside the strong lensing regime with the ground based data (beyond ~ 500 kpc) the determination of redshift distribution will become much more important.

5. X-RAY DATA REDUCTION

Under the assumptions of hydrostatic equilibrium and spherical symmetry, one can use the observed X-ray surface brightness profile and the deprojected X-ray gas temperature profile to determine the total mass and gas

mass profile. The reduction and analysis of the Chandra X-ray data is described in detail by Allen et al. (2007), Schmidt & Allen (2007), and Million et al. (in preparation). The thermodynamic X-ray pressure map determined from the Chandra data (total clean exposure time 67.9ks) is shown in Fig. 3. Overall, the pressure map shows that the cluster is remarkably relaxed, although the localized region of high-pressure, shocked gas in the southeast quadrant discovered and discussed by Komatsu et al. (2001) and Allen et al. (2002) is also clearly visible (indicating recent merger activity).

The cluster mass profile was determined from the observed deprojected X-ray temperature (Fig. 3) and surface brightness profiles (see Schmidt & Allen 2007 for details). The data from the southeast quadrant (position angles of 180–280 degrees measured west-through-north) were excluded from this analysis. In order to compare with the lensing mass measurements presented in this paper, we have projected the three-dimensional mass (and later also gas) profile determined from the Chandra data, assuming that the cluster extends to the virial radius (as determined from the X-ray data), $R_{\text{vir}} = 3.03$ Mpc. To estimate the systematic errors arising from this choice of truncation radius, we adopt conservative limits and change the radius by 30%. This resulted in changes to the projected masses measured within 600kpc of the cluster center that are within the quoted uncertainties; the precise value for the truncation radius is therefore of limited importance for this study. The resulting projected integrated mass profile is plotted in Fig. 5 together with mass estimates obtained from lensing analysis.

6. CLUSTER MASS RECONSTRUCTION FROM STRONG AND WEAK LENSING DATA

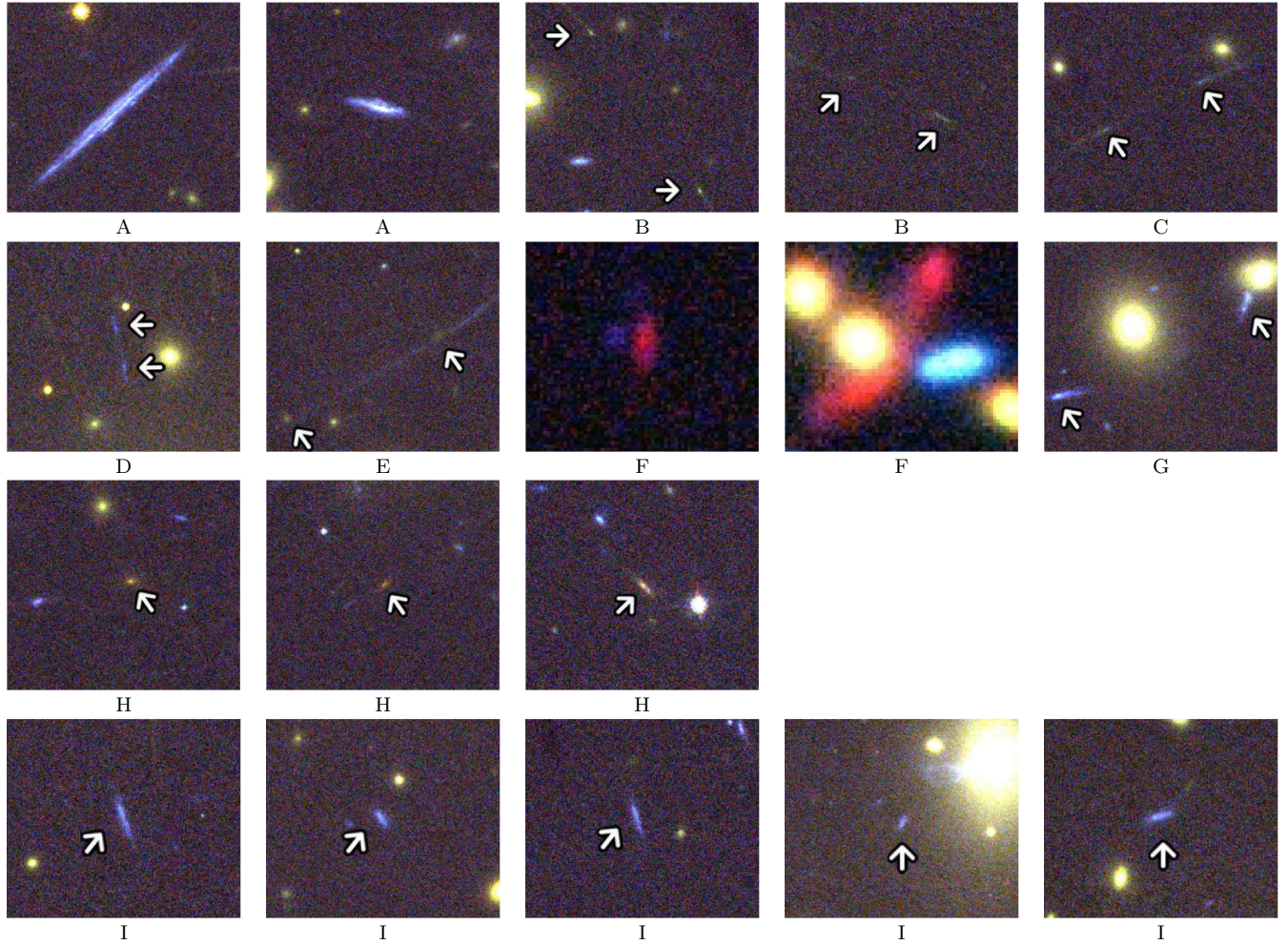


FIG. 2.— $10'' \times 10''$ cutouts of the multiply imaged systems from the F450W-F814W-F850LP color composite (except for image F, where BRK FORS data was used due to its extreme red color).

In this section we present the combined strong and weak lensing mass reconstruction of RX J1347.5–1145. Here we essentially follow the method described in Bradač et al. (2005b) and implemented on the ACS data in Bradač et al. (2006). The basic idea is to describe the cluster’s projected gravitational potential by a set of its values on a regular grid ψ_k , from which we evaluate all quantities relevant for gravitational lensing by finite differencing. E.g. the scaled surface mass density κ is related to ψ via Poisson equation, $2\kappa = \nabla^2\psi$ (where the physical surface mass density is $\Sigma = \kappa \Sigma_{\text{crit}}$ and Σ_{crit} is a constant that depends upon the angular diameter distances between the observer, the lens, and the source).

The advantage of such an approach is that we avoid making any assumption on e.g. shape and/or profile of the potential, which is crucial when dealing with merging clusters. The strong and weak lensing data are then combined in a χ^2 -fashion. We minimise the χ^2 by searching for the solution of the equation $\partial\chi^2/\partial\psi_k = 0$. We linearize the resulting system (using the initial values for the potential - see below - or values from the previous iteration) and solve it using sparse matrix techniques. Since the weak lensing data is noisy, regularisation (i.e. a process which ensures that unphysical pixel-to-pixel variations in surface mass density are suppressed) needs

to be employed. For this purpose we compare the current surface mass density map with one obtained on a coarser grid, and penalize strong deviations in χ^2 (see Bradač et al. 2005b for details). The regularisation is chosen (and tested to be) such as to not bias the resulting mass estimates.

6.1. Initial conditions of the method

For the purpose of obtaining the initial values of the potential needed in the first step of the iteration we assume a single singular isothermal sphere centered on the BCG with velocity dispersion $\sigma = 1600 \text{ km s}^{-1}$, taken from the strong lens modeling. As noted by Eliásdóttir et al. (2007) there is a non-trivial conversion between σ and σ_{PIEMD} ; therefore we simply assume a model with similar enclosed mass within the Einstein radius. We have chosen a more simplistic model than in §3 on purpose, in order not to bias our results and obtain a reconstruction independent of the assumptions about the potential (as is the case in assuming parametrised models). These particular assumptions, however, do not influence the results much, when high quality data, such as the ones here, are used (see discussion in §6.3). Therefore any reasonable guess for a cluster potential (from X-rays, dynamical mass estimate, etc) can be used.

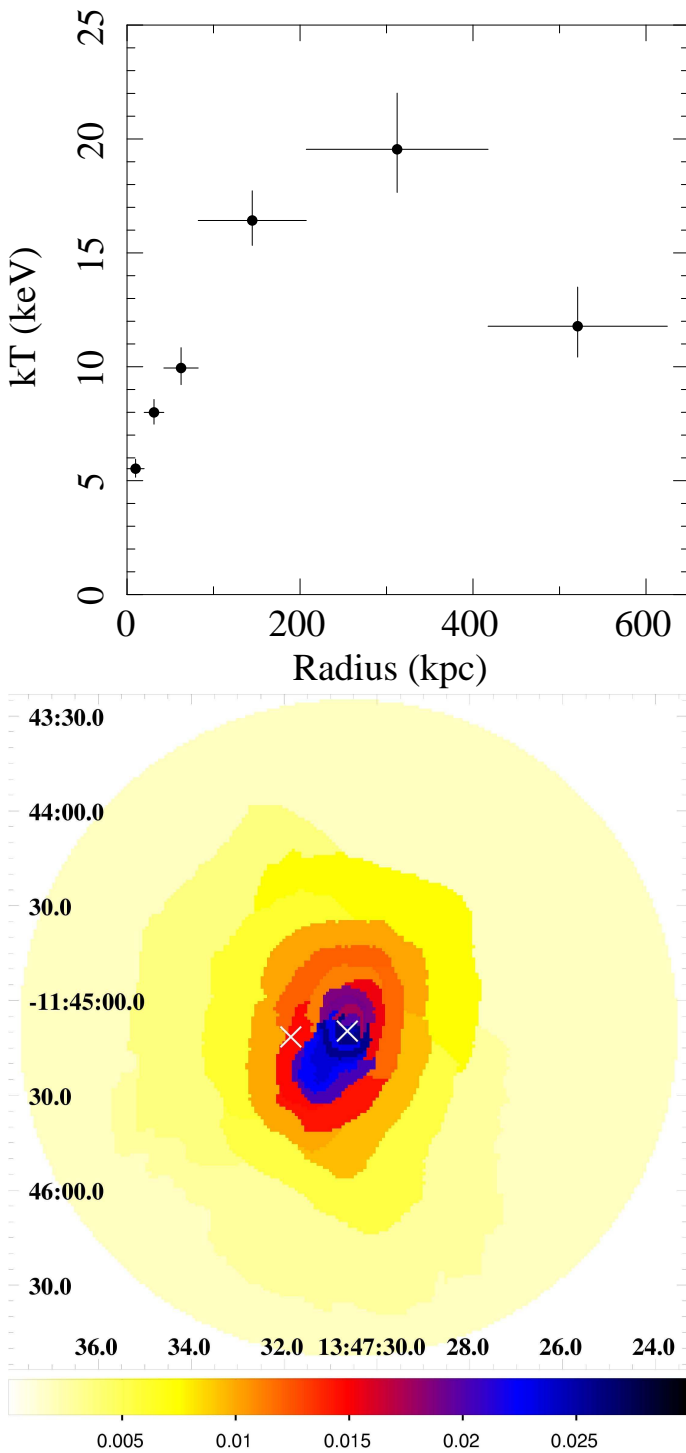


FIG. 3.— (top) The deprojected temperature profile of the X-ray emitting gas in RXJ1347.5–1145 determined from the Chandra X-ray data. The data from the southeast quadrant were excluded from the analysis, as described in the text. (bottom) The pressure map of RX J1347.5–1145. The two crosses indicate the two brightest cluster members.

6.2. Combined reconstruction

As described in section 3 we use 9 different multiply imaged systems and 700 weakly-lensed galaxies (70 arcmin^{-2}). We start with a $30 \times 30 \text{ pix}^2$ grid for a $4.2 \times 4.2 \text{ arcmin}^2$ field ($8''/\text{pix}$; the cluster is not centered

in the ACS field) oriented with respect to the negative RA coordinate (not all of the grid cells in the field contain data and those that do not are excluded from the reconstruction). We gradually increase the number of grid points in steps of 1, with the final reconstruction performed on a $60 \times 60 \text{ pix}^2$ ($4''/\text{pix}$) grid.

The resulting reconstruction is shown in Fig. 4, together with X-ray surface brightness contours from the Chandra observation (see Sect. 5). We clearly detect the main cluster component, which is aligned with the BCG. The offset from the BCG is $(-2'' \pm 2'', -1'' \pm 3'')$ and is also consistent with the peak of the X-ray surface brightness. We also resolve the south west structure, which also shows an overdensity of cluster members. The resulting model predicts the strongly lensed image positions with an average accuracy of less than $4''$, which is also effectively the final pixel size. In order to reach higher resolutions, adaptive grid methods need to be employed; this will be a subject of future work.

The mass profile, calculated by determining the enclosed, projected mass within circular apertures is plotted in Fig. 5. The errors include both systematic and statistical contributions, their estimation is described in more detail in Sect. 6.3. We fit power-law model ($M(< R) \propto R^n$) to the profile, and find it to poorly represent the data. The logarithmic slope of the best fit model is $n = 1.6 \pm 0.1$ (shallower than isothermal). Adopting an isothermal profile, we find a line-of-sight velocity dispersions for $\sigma = (1550 \pm 100) \text{ km s}^{-1}$.

The total mass profile is in excellent agreement with the X-ray data. It also agrees with the analysis in Bradač et al. (2005a), and strong lens modeling in Halkola et al. (2008) and the one presented in §3 (the data points using only strong lensing information in Fig 5 are extrapolated to a larger radius using the adopted profile for modelling). The agreement between our strong and strong and weak lensing modelling is expected, since for the analysis in §3 we use the same set of multiply imaged systems; Halkola et al. (2008) does use a subset of multiple images, and the agreement between these semi-independent analyses is very good. Most importantly, however, the agreement between X-ray data and lensing analyses was not achieved to this accuracy in the past and it is very encouraging to note that with excellent data we can indeed measure cluster masses reliably. Whereas the results from Bradač et al. (2005a) show that even with the ground-based data one can reliably measure enclosed mass, in order to obtain the full mass profile space-based data are required. In addition, as shown by Halkola et al. (2008), if using a reasonable guess for the cluster potential only a few systems are needed to reconstruct the mass profile. However, further image systems, and the addition of weak lensing data, increases the resolution and radial extent of the reconstruction, which helps breaking the degeneracies in the mass profile as shown in §7.

We also compare our estimates with the recent X-ray and gravitational lensing comparison of Gitti et al. (2007). The paper is based on old lensing data (the ACS/HST data is not included) together with XMM data. Whereas the lensing results have not changed significantly, there is a disagreement between Chandra and XMM X-ray data.

The X-ray results presented here are in excellent agreement with those reported by Allen et al. (2002) from a previous analysis of a Chandra data set with shorter exposure. The X-ray derived masses are larger than those reported from the analysis of XMM-Newton data by Gitti et al. (2007). The origin of this discrepancy is likely to lie at least in part in the complicating effects of the XMM-Newton point spread function, which are significant in the presence of strong temperature gradients (Fig. 3) and which were not modelled in detail by Gitti et al. (2007).

The largest circular aperture we can place on the BCG is 350 kpc. The enclosed, projected mass within this aperture is $M_L(< 350 \text{ kpc}) = (5.9 \pm 0.5) \times 10^{14} M_\odot$. The uncertainties include statistical as well as systematic errors, originating from weak lensing measurements, possible multiple image and redshift misidentification, and the initial model we used. We now describe the error budget in more detail.

6.3. Errors and Possible Systematic Effects

As in Bradač et al. (2006), we also extensively study possible errors and systematic effects. We generate 1000 bootstrap resampled weak lensing catalogs and perform reconstructions on each of these. To further test the reliability of the strong lensing data we create 9 different reconstructions, each time removing one of the multiply imaged systems we use. The resulting κ -maps do not change substantially, the main features (i.e. the ellipticity of the cluster and SW extension) seen in Fig. 4 remain in all of the reconstructions.

We have also run the reconstruction by changing the average redshift of weak lensing sources to $z_{WL} = 1.0$ and $z_{WL} = 2.0$. The changes in mass estimates were at the 1% level; hence the precise value of z_{WL} is unimportant in this case. The normalisation of the mass profile is determined by the much stronger signal coming from 9 multiple-image systems with “assumed” known redshifts. Weak lensing is helping here with the shape of the mass distribution in the areas where no multiply imaged systems are present.

Finally we study the dependence of the results on initial conditions. As noted in Bradač et al. (2006) the main features of the reconstruction are independent of the initial conditions we use. This is mostly attributed to the richness of the strong lensing data used in that paper and here. Still, we performed mass reconstructions where we changed the velocity dispersion of the initial model to $\sigma = 1900 \text{ km s}^{-1}$ and $\sigma = 1300 \text{ km s}^{-1}$; the resulting mass estimates are within the errors quoted above.

In summary, the errors on mass and surface mass density quoted throughout this paper include the errors obtained from bootstrap resampling the weak lensing catalogues, and removing individual strong lens systems (the latter dominate the error budget). The other errors discussed in this section have a minor contribution to the total error budget.

6.4. A Possible $z = 4.08$ System?

During their spectroscopy run, Cohen & Kneib (2002) serendipitously discovered a candidate $z = 4.08$ object (see Fig. 6). Using our final mass reconstruction we have

searched for counter images of this object, unfortunately without success. If present we would have expected multiple images to be easy to identify even in the absence of a reliable lens model, given its somewhat distinctive colors (see Figure 6). Furthermore, the object is fairly bright in the F475W filter ($m_{F475W,AB} = 25.55 \pm 0.03$) and has a relatively blue F475W-F814W color (1.46 ± 0.04). This new piece of information appears to be inconsistent with the suggested redshift of $z = 4.08$, since the flux shortwards of Lyman alpha should be absorbed by the Lyman alpha forest (Madau et al. 1996).

At present we can therefore neither confirm nor reject the possibility of this object being lensed. However, we think it is unlikely that the bright knot is indeed at a redshift of 4.08. Since we also see some underlying extended emission, it is possible that the bright knot is a foreground object and the extended object is being lensed; due to its low surface brightness we do not expect to be able to identify its counter images. A more likely possibility is that the emission line detected by Cohen & Kneib (2002) is the [O II] doublet at 3727Å, implying a redshift of $z = 0.66$ and therefore no multiple imaging. We do not expect the doublet to be resolved given the spectral resolution of $\sim 10\text{\AA}(\text{FWHM})$. We conclude that the redshift of this object is uncertain at present and further investigations are needed to either confirm or reject the present redshift estimate.

7. DISSECTING RX J1347.5–1145 INTO DARK MATTER AND BARYONS

The relative distribution of dark matter and baryons in galaxy clusters is important for a number of reasons. Whereas baryons are only a minor total mass constituent in the dark matter dominated clusters, in the centres of the clusters baryons are an important mass component. In order to make a proper comparison with Λ CDM predictions we need to disentangle both components. The interplay between baryons and dark matter is important and can potentially change the inner slope of dark matter halos (see e.g. Gnedin et al. 2004). Therefore in this section we separate the total mass measurements we obtain from gravitational lensing analysis into baryonic (gas and stars) and non-baryonic component and measure the dark matter distribution of RX J1347.5–1145.

7.1. 2-D distribution of dark matter and baryons

To estimate the stellar mass distribution we first estimate the cluster K-band luminosity distribution by selecting the cluster members using the photometric redshift (obtained using information from 8 colors from ground-based data in Bradač et al. 2005a) cuts at $[0.3 - 0.55]$. We measure their K-band luminosity by assuming the absolute solar magnitude $M_{K,\odot} = 3.28$, galactic extinction following Schlegel et al. (1998) and Cardelli et al. (1989) of $A_K = 0.023$, and K-correction from Poggianti (1997) of $K_K(z_d) = -0.25$. We smooth the distribution using a Gaussian kernel of FWHM of 30kpc. To convert the stellar luminosity into stellar mass we follow Drory et al. (2004) and assume the stellar-mass-to-light ratio in K-band to be $M_*/L_K = 0.74 \pm 0.3$ (see also Bell et al. 2003).

The stellar K-band luminosity is shown in Fig. 4 in white contours. It follows the total mass distribution considerably well, we detect the SW extension in both

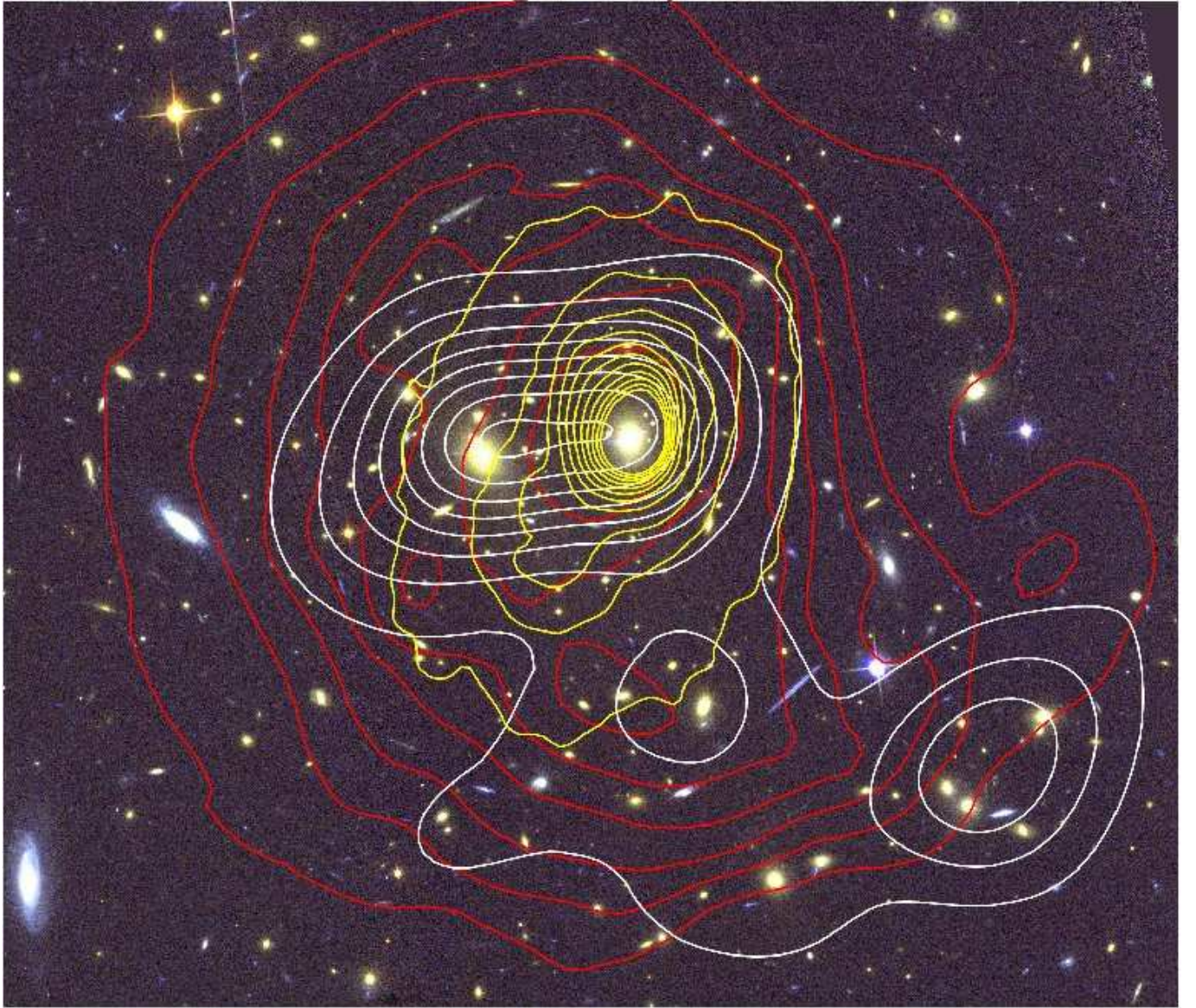


FIG. 4.— The F450W-F814W-F850LP color composite of the cluster RX J1347.5–1145. Overlaid in *red contours* is the surface mass density κ from the combined weak and strong lensing mass reconstruction. The contour levels are linearly spaced with $\Delta\kappa = 0.2$, starting at $\kappa = 0.5$, for a fiducial source at a redshift of $z_s \rightarrow \infty$. The X-ray brightness contours (also linearly spaced) are overlaid in *yellow* and the K-band light (tracing the stellar mass) is overlaid in *white*. North is up and East is left, the field is $2.3' \times 2.3'$, which corresponds to $800 \times 800 \text{ kpc}^2$ at the redshift of the cluster.

cases. Also shown is the X-ray surface brightness, indicating that the major baryonic component is spatially aligned with the distribution of the total mass and hence dark matter within the uncertainties.

7.2. Projected density profile of dark matter and baryons

In Fig. 7 we present the total surface (projected) mass density profile Σ from the lensing reconstruction. Further we obtain the dark matter profile by subtracting the stellar and gas density profile from the total density profile, as described next.

The stellar mass profile is obtained from the 2-D K-band light distribution. We assume the dominant source of error comes from the uncertainty of M_*/L_K . We again smooth the distribution using a Gaussian kernel of FWHM of 30 kpc; the exact value is of lesser importance here, since stars contribute a minor fraction of the total

baryonic mass at radii $\gtrsim 50$ kpc and we are not sensitive in smaller scale variations in the total mass profile.

The projected gas profile is obtained from the observed X-ray surface brightness profile and the deprojected X-ray gas temperature profile. Finally, the dark matter profile is calculated from the difference between the baryonic and the total mass profile from strong and weak lensing mass reconstruction. In Fig. 7 we show the individual contributions of stars, gas, and dark matter.

To estimate the inner slope of the dark matter halo we fit a generalized, projected NFW profile: the 3D density is given by

$$\rho_{\text{DM}}(r) = \frac{\rho_{0,\text{DM}}}{(r/r_s)^\beta (1+r/r_s)^{3-\beta}}. \quad (1)$$

We determine the asymptotic inner slope β , the scale radius r_s and the normalisation $\rho_{0,\text{DM}}$ from the data given in Fig. 7. We assume a flat prior $\beta > 0$, since negative

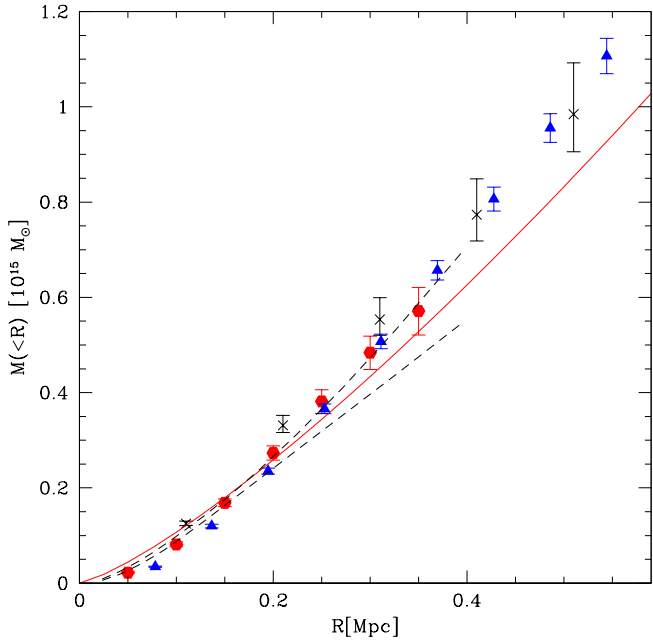


FIG. 5.— The integrated, projected mass profile of RX J1347.5–1145. The profile was determined by measuring the enclosed mass in cylinders, centered on the BCG using strong and weak lensing (hexagons), strong lensing using parametrised model (triangle) and X-ray data (crosses). We fit power law profiles to the strong and weak lensing data, the result is shown as a solid line. 1-sigma error region from the results obtained by Halkola et al. (2008) using only strong lensing data is shown as dashed lines.



FIG. 6.— $10'' \times 10''$ cutout of the $z = 4.08$ candidate discovered by Cohen & Kneib (2002) from the F450W-F814W-F850LP color composite.

values of β give unphysical profiles. When fitting the profile we include the full covariance matrix (i.e. taking into account correlations between the bins) for the

estimate of the total density, gas density and the stellar mass density. The covariance matrix was determined directly from strong and weak lensing bootstrap resampled reconstructions and by sampling the models given the uncertainties from gas and stellar mass measurements. We note however, that another potential source of systematic errors will arise from the lack of the symmetry in the mass distribution and somewhat complicated geometry of this system. There is also the ambiguity when choosing the center of mass for the profile estimation, which should be computed around the center of mass. We chose to center the profile on the BCG, which is a good approximation in our case, since the maximum of Σ is consistent with the position of the BCG ($2'' \pm 4''$, i.e. < 10 kpc).

Furthermore, as already noted by Sand et al. (2007) there are strong degeneracies between the generalised NFW parameters. In particular we found a strong degeneracy between the scale radius r_s and the inner slope β . The best fit profile gives $\beta = 0.0 \pm 0.1$ and $r_s = 160$ kpc ± 10 kpc ($c_{200} = 15$ and $r_{200} = 2400$ kpc). However, as shown in Fig. 7 the NFW profile fit with a fixed inner slope $\beta = 1$ is not significantly worse. The latter gives a scale radius of $r_s = 350$ kpc ± 100 kpc ($c_{200} = 6$ and $r_{200} = 2200$ kpc). The statistical uncertainties alone on c_{200} are of the order of $\sim 20\%$.

To reliably determine the concentration parameter and hence β we therefore need the data to extend to much larger scales (i.e. beyond r_{vir}). Strong lensing data alone (for this and also all the other clusters) are not sufficient for this task. We plan to extend this analysis by adding wide field weak lensing data that extend to a radius of $\sim 30'$ (10 Mpc); this will be a subject of a forthcoming paper.

Finally, the thermodynamic X-ray pressure map (Fig. 3) shows the localized region of high-pressure, shocked gas in the southeast quadrant. Therefore we are likely measuring a profile of two post-merging, unequal mass clusters. This is further supported by the presence of the eastern cD galaxy. Therefore the cluster might not be fully relaxed and therefore the measurement of the total dark matter distribution is unlikely to follow the NFW profile in great detail at these small radii.

8. CONCLUSIONS AND OUTLOOK

The longstanding puzzle of the discrepant mass estimates for the most X-ray luminous cluster seems to be definitely resolved. Both our strong and weak lensing as well as X-ray mass reconstructions agree well. In particular we draw the following conclusions:

1. Using the combined strong and weak lensing mass reconstruction we derive a high-resolution, absolutely calibrated mass map; we get projected, enclosed mass $M_L(< 350\text{kpc}) = (5.9 \pm 0.5) \times 10^{14} M_\odot$. Within the same radius the projected mass derived from X-ray data alone is $M_X(< 350 \text{ kpc}) = (6.6^{+0.6}_{-0.4}) \times 10^{14} M_\odot$.
2. The mass estimates are still in disagreement with previous dynamical mass estimates by Cohen & Kneib (2002). It is however possible that Cohen & Kneib (2002) measured the velocity dispersion of the infalling subcluster only (Allen et al.

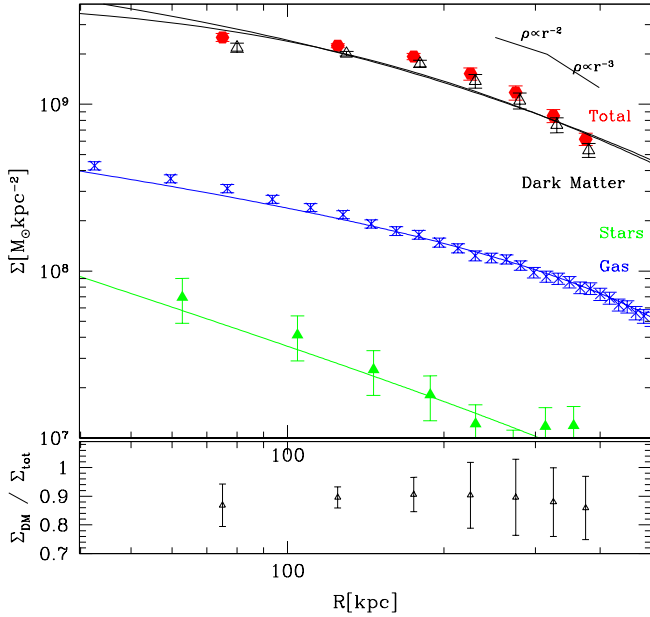


FIG. 7.— (top) The projected mass density Σ profile of RX J1347.5–1145 showing separately the stellar profile (filled triangles - green), the gas profile (stars - blue), dark matter profile (open triangles - black) and the total profile as measured from strong and weak lensing (hexagons - red). The dark matter profile has been fitted using the generalised NFW (cf. Eq. 1) - shown is the best fit model ($\beta = 0$, $r_s = 160$ kpc) and a best fit NFW model ($\beta = 1$, $r_s = 350$ kpc). For gas and stars we use simple power law profiles. Also shown for reference are the Σ -profiles for 3D density profiles $\rho \propto r^{-2}$ and $\rho \propto r^{-3}$. Dark matter points have been offset in the R-direction for clarity. (bottom) The ratio of dark matter to total matter.

2002), thereby biasing the mass estimate low. If taken as a measurement of the cluster mass, such a low velocity dispersion cluster is in complete disagreement with strong lensing features we observe (regardless of their redshift). We are currently analysing the remainder of spectroscopy data to resolve this issue (Lombardi et al. in preparation).

3. Using the exquisite resolution of ACS data we are able to study the spatial distribution of dark matter with respect to the baryons at unprecedented accuracy. We clearly detect a mass concentration centered on the BCG and a SW extension, which follows the light distribution of the cluster members. Further we fit a generalised NFW model to

the dark matter density profile, finding strong degeneracies between the inner slope β and the scale radius r_s . Our data does not extend to sufficiently large radii, for more secure determination of β , r_s , and concentration parameter; we plan to use weak lensing data extending beyond the virial radius in the future to resolve this issue.

The cluster RX J1347.5–1145 is an extremely valuable object for understanding the details of cluster formation and evolution. In addition, due to their magnifying power, these most massive clusters are ideal tools to study the high-redshift universe. By searching around the critical line for high redshift sources as predicted by our lens model we were already able to find high redshift multiple imaged systems. We plan to extend this search in the future.

The large wavelength coverage of the data for this cluster has proved to be extremely valuable for a detailed study of the cluster mass distribution. With such data sets most massive clusters of galaxies remain one of the key objects to constrain cosmological parameters and to study the galaxy formation and evolution from the early times until the present.

We would like to thank Masamune Oguri for many useful discussions. Support for this work was provided by NASA through grant number HST-GO-10492.03A from the Space Telescope Science Institute, which is operated by AURA, Inc., under NASA contract NAS 5-2655. This research has made use of data obtained from the Chandra Data Archive and software provided by the Chandra X-ray Center (CXC). MB acknowledges support from the NSF grant AST-0206286 and from NASA through Hubble Fellowship grant # HST-HF-01206.01 awarded by the Space Telescope Science Institute. TT acknowledges support from the NSF through CAREER award NSF-0642621, by the Sloan Foundation through a Sloan Research Fellowship, and by the Packard Foundation through a Packard Fellowship. This work was supported by the Deutsche Forschungsgemeinschaft under the project SCHN 342/3–1 and the German Ministry for Science and Education (BMBF) under the projects 05AV5PDA/3 and 50 OR 0601. This project was also partially supported by the Department of Energy contract DE-AC3-76SF00515 to SLAC.

REFERENCES

Allen, S. W., Rapetti, D. A., Schmidt, R. W., Ebeling, H., Morris, G., & Fabian, A. C. 2007, arXiv:astro-ph/0706.0033

Allen, S. W., Schmidt, R. W., & Fabian, A. C. 2002, MNRAS, 335, 256

Anderson, J. & King, I. R. 2006, in ACS Instrument Science Report 2006-01

Bell, E. F., McIntosh, D. H., Katz, N., & Weinberg, M. D. 2003, ApJS, 149, 289

Bertin, E. & Arnouts, S. 1996, A&AS, 117, 393

Bradač, M., Clowe, D., Gonzalez, A., Marshall, P., Forman, W., Jones, C., Markevitch, M., Randall, S., Schrabback, T., & Zaritsky, D. 2006, ApJ, 652, 937

Bradač, M., Erben, T., Schneider, P., Hildebrandt, H., Lombardi, M., Schirmer, M., Schindler, S., & Miralles, J.-M. 2005a, A&A, 437, 49

Bradač, M., Schneider, P., Lombardi, M., & Erben, T. 2005b, A&A, 437, 39

Bradač, M., Schneider, P., Lombardi, M., Steinmetz, M., Koopmans, L. V. E., & Navarro, J. F. 2004, A&A, 423, 797

Broadhurst, T., Benítez, N., Coe, D., Sharon, K., Zekser, K., White, R., Ford, H., et al. 2005, ApJ, 621, 53

Cacciato, M., Bartelmann, M., Meneghetti, M., & Moscardini, L. 2005, astro-ph/0511694

Cardelli, J. A., Clayton, G. C., & Mathis, J. S. 1989, ApJ, 345, 245

Cohen, J. G. & Kneib, J. 2002, ApJ, 573, 524

Diego, J. M., Tegmark, M., Protopapas, P., & Sandvik, H. B. 2005, *astro-ph/0509103*

Drory, N., Bender, R., Feulner, G., Hopp, U., Maraston, C., Snigula, J., & Hill, G. J. 2004, *ApJ*, 608, 742

Elíasdóttir, Á., Limousin, M., Richard, J., Hjorth, J., Kneib, J.-P., Natarajan, P., Pedersen, K., Jullo, E., & Paraficz, D. 2007, *ArXiv e-prints*, 710

Ettori, S., Tozzi, P., Borgani, S., & Rosati, P. 2004, *A&A*, 417, 13

Falco, E. E., Gorenstein, M. V., & Shapiro, I. I. 1985, *ApJ*, 289, L1

Fischer, P. & Tyson, J. A. 1997, *AJ*, 114, 14

Gitti, M., Piffaretti, R., & Schindler, S. 2007, *A&A*, 472, 383

Gitti, M. & Schindler, S. 2004, *A&A*, 427, L9

Gnedin, O. Y., Kravtsov, A. V., Klypin, A. A., & Nagai, D. 2004, *ApJ*, 616, 16

Halkola, A., Hildebrandt, H., Schrabback, T., Lombardi, M., Bradac, M., Erben, T., Schneider, P., & Wuttko, D. 2008, *ArXiv e-prints*, 801

Halkola, A., Seitz, S., & Pannella, M. 2006, *MNRAS*, 372, 1425

Heymans, C., Brown, M. L., Barden, M., Caldwell, J. A. R., Jahnke, K., Peng, C. Y., Rix, H.-W., Taylor, A., Beckwith, S. V. W., Bell, E. F., Borch, A., Häubler, B., Jogee, S., McIntosh, D. H., Meisenheimer, K., Sánchez, S. F., Somerville, R., Wisotzki, L., & Wolf, C. 2005, *MNRAS*, 361, 160

Heymans, C., Van Waerbeke, L., Bacon, D., Berge, J., Bernstein, G., Bertin, E., Bridle, S., Brown, M. L., Clowe, D., Dahle, H., Erben, T., Gray, M., Hetterscheidt, M., Hoekstra, H., Hudelot, P., Jarvis, M., Kuijken, K., Margoniner, V., Massey, R., Mellier, Y., Nakajima, R., Refregier, A., Rhodes, J., Schrabback, T., & Wittman, D. 2006, *MNRAS*, 368, 1323

Hoekstra, H., Franx, M., Kuijken, K., & Squires, G. 1998, *ApJ*, 504, 636

Jee, M. J., Ford, H. C., Illingworth, G. D., White, R. L., Broadhurst, T. J., Coe, D. A., Meurer, G. R., van der Wel, A., Benitez, N., Blakeslee, J. P., Bouwens, R. J., Bradley, L. D., Demarco, R., Homeier, N. L., Martel, A. R., & Mei, S. 2007, *ApJ*, 661, 728

Jee, M. J., White, R. L., Ford, H. C., Illingworth, G. D., Blakeslee, J. P., Holden, B., & Mei, S. 2006, *ApJ*, 642, 720

Jullo, E., Kneib, J.-P., Limousin, M., Elíasdóttir, Á., Marshall, P., & Verdugo, T. 2007, *arXiv:astro-ph/0706.0048*

Kaiser, N., Squires, G., & Broadhurst, T. 1995, *ApJ*, 449, 460

Kitayama, T., Komatsu, E., Ota, N., Kuwabara, T., Suto, Y., Yoshikawa, K., Hattori, M., & Matsuo, H. 2004, *PASJ*, 56, 17

Kneib, J., Hudelot, P., Ellis, R. S., Treu, T., Smith, G. P., Marshall, P., Czoske, O., Smail, I., & Natarajan, P. 2003, *ApJ*, 598, 804

Kneib, J. P., Mellier, Y., Fort, B., & Mathez, G. 1993, *A&A*, 273, 367

Koekemoer, A. M., Fruchter, A. S., Hook, R. N., & Hack, W. 2002, in *The 2002 HST Calibration Workshop*, Baltimore, MD, 2002., p.339, 339

Komatsu, E., Matsuo, H., Kitayama, T., Hattori, M., Kawabe, R., Kohno, K., Kuno, N., Schindler, S., Suto, Y., & Yoshikawa, K. 2001, *PASJ*, 53, 57

Krist, J. E. 2003, in *ACS Instrument Science Report 2003-06*

Limousin, M., Kneib, J.-P., & Natarajan, P. 2005, *MNRAS*, 356, 309

Limousin, M., Richard, J., Jullo, E., Kneib, J.-P., Fort, B., Soucail, G., Elíasdóttir, Á., Natarajan, P., Ellis, R. S., Smail, I., Czoske, O., Smith, G. P., Hudelot, P., Bardeau, S., Ebeling, H., Egami, E., & Knudsen, K. K. 2007, *ApJ*, 668, 643

Lombardi, M. et al. 2007, *in preparation*

Luppino, G. A. & Kaiser, N. 1997, *ApJ*, 475, 20

Lupton, R., Blanton, M. R., Fekete, G., Hogg, D. W., O'Mullane, W., Szalay, A., & Wherry, N. 2004, *PASP*, 116, 133

Madau, P., Ferguson, H. C., Dickinson, M. E., Giavalisco, M., Steidel, C. C., & Fruchter, A. 1996, *MNRAS*, 283, 1388

Massey, R. & Goldberg, D. M. 2007, *arXiv:astro-ph/0709.1479*

Massey, R., Rhodes, J., Ellis, R., Scoville, N., Leauthaud, A., Finoguenov, A., Capak, P., Bacon, D., Aussel, H., Kneib, J.-P., Koekemoer, A., McCracken, H., Mobasher, B., Pires, S., Refregier, A., Sasaki, S., Starck, J.-L., Taniguchi, Y., Taylor, A., & Taylor, J. 2007, *Nature*, 445, 286

Nagai, D. & Kravtsov, A. V. 2005, *ApJ*, 618, 557

Natarajan, P. & Kneib, J.-P. 1996, *MNRAS*, 283, 1031

Navarro, J. F., Frenk, C. S., & White, S. D. M. 1997, *ApJ*, 490, 493

Navarro, J. F., Hayashi, E., Power, C., Jenkins, A. R., Frenk, C. S., White, S. D. M., Springel, V., Stadel, J., & Quinn, T. R. 2004, *MNRAS*, 349, 1039

Neto, A. F., Gao, L., Bett, P., Cole, S., Navarro, J. F., Frenk, C. S., White, S. D. M., Springel, V., & Jenkins, A. 2007, *MNRAS*, 381, 1450

Poggianti, B. M. 1997, *A&AS*, 122, 399

Pointecouteau, E., Giard, M., Benoit, A., Désert, F. X., Bernard, J. P., Coron, N., & Lamarre, J. M. 2001, *ApJ*, 552, 42

Ravindranath, S. & Ho, L. C. 2002, *ApJ*, 577, 133

Rhodes, J. D., Massey, R. J., Albert, J., Collins, N., Ellis, R. S., Heymans, C., Gardner, J. P., Kneib, J.-P., Koekemoer, A., Leauthaud, A., Mellier, Y., Refregier, A., Taylor, J. E., & Van Waerbeke, L. 2007, *ApJS*, 172, 203

Sahu, K. C., Shaw, R. A., Kaiser, M. E., Baum, S. A., Ferguson, H. C., Hayes, J. J. E., Gull, T. R., Hill, R. J., Hutchings, J. B., Kimble, R. A., Plait, P., & Woodgate, B. E. 1998, *ApJ*, 492, L125

Sand, D. J., Treu, T., Ellis, R. S., Smith, G. P., & Kneib, J. 2007, *arXiv:astro-ph/0710.1069*

Schindler, S., Guzzo, L., Ebeling, H., Boehringer, H., Chincarini, G., Collins, C. A., de Grandi, S., Neumann, D. M., Briel, U. G., Shaver, P., & Vettolani, G. 1995, *A&A*, 299, L9

Schindler, S., Hattori, M., Neumann, D. M., & Boehringer, H. 1997, *A&A*, 317, 646

Schlegel, D. J., Finkbeiner, D. P., & Davis, M. 1998, *ApJ*, 500, 525

Schmidt, R. W. & Allen, S. W. 2007, *MNRAS*, 379, 209

Schneider, P. & Seitz, C. 1995, *A&A*, 294, 411

Schrabback, T., Erben, T., Simon, P., Miralles, J.-M., Schneider, P., Heymans, C., Eifler, T., Fosbury, R. A. E., Freudling, W., Hetterscheidt, M., Hildebrandt, H., & Pirzkal, N. 2007, *A&A*, 468, 823

Sharon, K., Ofek, E. O., Smith, G. P., Broadhurst, T., Maoz, D., Kochanek, C. S., Oguri, M., Suto, Y., Inada, N., & Falco, E. E. 2005, *ApJ*, 629, L73

Smith, G. P., Kneib, J., Smail, I., Mazzotta, P., Ebeling, H., & Czoske, O. 2004, *astro-ph/0403588*